UDC 621.315.592

Local doping of monolayer WSe_2 on piezoelectric $GaInP_2$ and GaN substrates

© V.Yu. Axenov, A.V. Ankudinov, A.S. Vlasov, M.S. Dunaevsky, V.N. Jmerik, D.V. Lebedev, K.V. Likhachev, V.A. Pereskokova, A.M. Mintairov¶

Ioffe Institute,
194021 St. Petersburg, Russia
¶ E-mail: amintairov@mail.ioffe.ru

Received April 19, 2024
Revised October 27, 2024
Accepted October 27, 2024

Non-contact local doping of monolayer WSe_2 transferred to piezoelectric epitaxial structures based on $InP/GaInP_2$ and GaN, having surface potential variations with an amplitude of $\sim 0.1\,B$ and a size of $\sim 0.2-1\,\mu m$ is shown. Using scanning probe microscopy surface potential measurements, as well as optical reflectance, photoluminescence, and Raman spectroscopy measurements we observed variations in charged exciton (trion) emission/reflectance and Raman intensity due to variations in the surface potential of WSe_2 monolayers, indicating local doping at $n \sim 10^{12}\,cm^{-2}$. Our results can be used to create Wigner quantum dots in transition metal dichalcogenides, which is promising for the development of fault-tolerant topological quantum computing at room temperature and without a magnetic field.

Keywords: 2D semiconductors, local doping, optical spectroscopy, Kelvin probe, microscopy.

DOI: 10.61011/SC.2024.08.59886.6252H

1. Introduction

Electrons in two-dimensional (2D) structures may couple to magnetic-flux quanta vortices to form composite particles (anyons) with fractional quantum statistics [1], which may be used to implement fault-tolerant topological quantum computing [2–4]. Anyons form in a transverse magnetic field in the fractional quantum Hall effect regime, which was observed in GaAs/AlGaAs [5], Si/Ge [6], MgZnO/ZnO [7], and GaN/AlGaN [8] semiconductor heterostructures and in atomically thin 2D materials [9], such as graphene [10] and transition metal dichalcogenides WSe_2 [11]. In quantum-confined structures (i.e., quantum puddles, which are islands containing several electrons), anyons may form in zero magnetic field in the Wigner localization regime. This was observed in GaAs/AlGaAs quantum wires [12], $InP/GaInP_2$ quantum dots [4], and impurity centers of Fe(Te,Se) topological superconductors [13]. The Wigner localization regime is established at a relatively low density n of electrons when the average distance between them exceeds the Bohr radius (a_B^*), which corresponds to dimensionless Wigner–Seitz radius $r_s = 1/[a_B^*(\pi \cdot n)^{0.5}] > 1$ and temperatures $T < \hbar\omega_0/k$, where $\hbar\omega_0$ is the quantum confinement energy and k is the Boltzmann constant. In semiconductor heterostructures, this regime is established at $n \sim 10^{10}\,cm^{-2}$ and helium temperatures [4,11,12]. Wigner localization is enhanced significantly in transition metal dichalcogenides (MoS_2, WSe_2, etc.) due to a low permittivity and a relatively large effective electron mass, which is provided by d shells of a transition metal [14]. Thus, fractional quantum Hall effect states in monolayer (1M) WSe_2 were observed at $n \sim 10^{12}\,cm^{-2}$ [10], which corresponds to $r_s \sim 3$ and quantum confinement energy $\hbar\omega_0 \sim 50\,meV$ and ensures the presence of anyons at room temperature. However, experimental measurements of tunnel transport (Coulomb blockade) in 1M-WSe_2 quantum dots formed by electrostatic gates reveal an order of magnitude lower $\hbar\omega_0$ values and suppression of single-electron tunnel transitions [15,16], indicating a high density of defects induced by the contact deposition process [15]. Thus, the development of contactless local doping methods, which may reduce the defect density significantly, is highly relevant to the implementation of anyonic quantum puddles in transition metal dichalcogenides.

In the present study, we propose and implement a contactless method for selective *in situ* local doping of transition metal dichalcogenide flakes with the use of piezoelectric substrates with surface potential wells induced by structural inhomogeneities. These inhomogeneities act as fixed built-in gates that pull electrons/holes from adjacent flake/substrate regions and ensure the formation of Wigner islands for wells of the corresponding size and depth. This makes it unnecessary to use metal nanoelectrodes and the corresponding process procedures to produce quantum puddles, allowing one to examine their properties via contactless optical techniques. Specifically, local doping may be controlled via photoluminescence (PL) spectra by monitoring the charged exciton (trion) peak emission intensity [14,17]. Three types of piezoelectric substrates, namely $GaInP_2$, $InP/GaInP_2$, and GaN, were used to transfer 1M-WSe_2 flakes and subjected to measurements of the surface potential, exciton reflectance spectra, confocal PL,

and Raman scattering (RS). Our measurement and analysis data reveal local 1M-WSe_2 doping up to $n \sim 10^{12}\,\mathrm{cm}^{-2}$ in regions $0.2-1\,\mu$m in size induced by structural inhomogeneities of piezoelectric substrates. This points the way toward the production of self-organized anyons in atomically thin 2D semiconductors and is essential for zero-field room-temperature topological quantum computing.

2. Object under study and research methods

Structures with $GaInP_2$ layers with thickness $d = 70-1500$ nm were grown on a GaAs substrate oriented along the [001] direction at a temperature of 720°C by metalorganic vapor-phase epitaxy and had the $CuPt_B$-type ordering of Ga and In atoms, which corresponds to a rhombohedral monolayer InP_1/GaP_1 superlattice oriented along the $[111]_B$ directions and featuring a built-in electric field [18].

In the process of epitaxial growth of InP/$GaInP_2$ structures, ~ 3 InP monolayers were deposited onto a 500-nm-thick $GaInP_2$ layer and overgrown with a 40-nm-thick $GaInP_2$ layer. InP islands (quantum dots) were formed at a depth of 40 nm as a result. These had a diameter of ~ 100 nm, a height of ~ 10 nm, and a density of $5\,\mu\mathrm{m}^{-2}$ [19]. Local strain in such a structure induces inhomogeneities of the surface potential that ensures electronic doping of InP dots [20].

Structures with N-polar GaN layers $\sim 1\,\mu$m in thickness were grown directly on c-Al_2O_3 by plasma-assisted molecular beam epitaxy at a temperature of 690°C under metal enrichment conditions with an effective flux ratio of $Ga/N_2 = 1.1-1.3$ [21]. GaN layers contained vertical inversion domains (i. e., inclusions with an opposite Ga polarity) penetrating through the entire layer and inducing surface potential wells. At a flux ratio of 1.3, gallium droplets with a size up to several micrometers and a density of $0.1\,\mu\mathrm{m}^{-2}$ formed on the layer surface.

Monolayer WSe_2 flakes were exfoliated mechanically from a bulk single crystal and transferred to $GaInP_2$, InP/$GaInP_2$, and GaN structures with the use of polydimethylsiloxane adhesive (scotch) tape. Test substrates (SiO_2/Si layers 300 nm in thickness) were also used.

Topography and surface potential maps of the obtained structures were measured with a spatial resolution of ~ 200 nm with an NTEGRA Aura atomic force microscope (NT-MDT SI, Russia) with Kelvin probes in accordance with the procedure outlined in [18]. PL and Raman spectra and intensity maps were measured and analyzed using a confocal microscope (Spectra NT-MDT SI) and the embedded IA_P9 software. The microscope was fitted with a spectrometer (SOL Instruments) and a CCD matrix (Andor). Spectra were excited by a semiconductor laser with a wavelength of $\lambda = 532$ nm ($\hbar\omega = 2.33$ eV) and a power of 5 mW. Emitted/scattered light from the sample was collected by an objective with a numerical aperture of 0.7 and a 100-μm-wide entrance aperture, which provided a signal collection volume $< 5\,\mu\mathrm{m}^3$ and a spatial resolution close to a micrometer. To record reflectance spectra, light from a halogen lamp was condensed into single-mode fiber. A parallel flux was produced by a lens system at the fiber output and introduced via a beam splitter into a confocal circuit used to measure the PL spectra. The irradiated region was several micrometers in diameter.

Built-in electric field E_{PE} of $GaInP_2$ layers was calculated as $E_{\mathrm{PE}} = (U_{s0} - U_{\mathrm{GaAs}})/d$, where U_{s0} is the surface potential of the layer averaged over the sample area and $U_{\mathrm{GaAs}} = 1.1$ V is the substrate potential measured in the $(1\bar{1}0)$ cleavage surface potential maps.

Examining the optical spectra, we measured position ν/λ, full width at half maximum γ, and intensity I of the phonon peak in the Raman spectra and the exciton/trion peak in the PL/reflectance spectra of 1M-WSe_2 flakes. The spatial variation of these parameters with surface potential U_s was also studied. The PL peak position was used to identify 1M and 2M flakes. Local doping was assessed by monitoring the intensity ratio of the exciton and trion peaks [17] (the latter is dominant in the PL/reflectance spectra at $n \sim 10^{12}\,\mathrm{cm}^{-2}$).

3. Main results

3.1. Piezoelectric properties of substrates

The results of measurements for $GaInP_2$ layers revealed that the surface potential U_{s0} values determined at the same thickness have a spread of 0.2–2.4 V, which corresponds to a built-in field E_{PE} spread from ± 100 to ± 7 kV/cm and is illustrated in Figure 1, *a* for $d = 70$, 250, 500, and 1500 nm. The spread of E_{PE} values is due to the differences in relaxation of $CuPt_B$ atomically ordered domains and to the switching between strained (cubic) and relaxed (rhombohedral) atom arrangements that occurs when the sample is chipped or, in other words, in the course of a martensitic transformation [22]. In addition, $|E_{\mathrm{PE}}|$ decreases by an order of magnitude as d increases from 70 to 1500 nm. This is attributable to pinning of the Fermi level, which is characterized by function $E_{\mathrm{PE}}(d) = Eg/4/(d + d_0)$, where E_g is the band gap of $GaInP_2$ (1.9 eV) and $d_0 = 20$ nm ($E_{\mathrm{PE}} > 0$ is shown in Figure 1, *a*). Fermi level pinning corresponds to piezoelectric doping, since $E_{\mathrm{PE}} > 0$ ($E_{\mathrm{PE}} < 0$) shifts the valence (conduction) band to the Fermi level, and a degenerate density is reached with $|E_{\mathrm{PE}}| = 100$ kV/cm already at $d = 150$ nm.

Probe microscopy measurements reveal that the surface potential U_s relief of $GaInP_2$ layers depends only weakly on E_{PE} and d and features shallow surface potential wells (SPWs) with depth $\Delta U_s \sim 0.01$ V, a size of ~ 100 nm, and a density of $\sim 5\,\mu\mathrm{m}^{-2}$ (see the U_s map for $d = 500$ nm in the upper inset in Figure 1, *a*).

In InP/$GaInP_2$ structures, the U_s relief undergoes significant changes: the size of SPWs increases to 200 nm, their

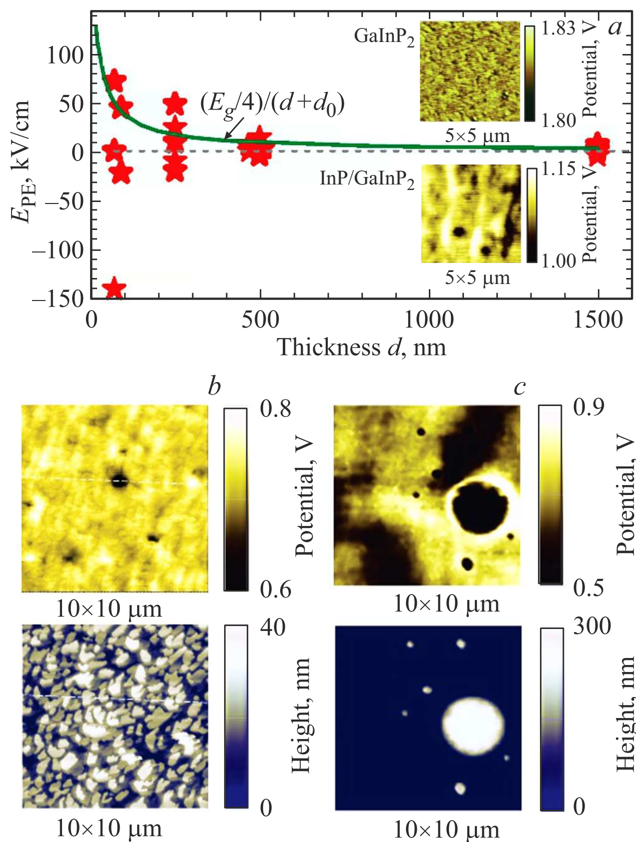

Figure 1. Dependence of the built-in electric field (EPE) of $GaInP_2$ layers on thickness d (experimental and calculated data are represented by asterisks and the curve, respectively) for Fermi level pinning $E_g/4$, where $E_g = 1.9$ eV is the band gap of $GaInP_2$ and $d_0 = 20$ nm (a); surface potential map ($5 \times 5\,\mu m^2$ in size) of the $GaInP_2$ layer with $d = 500$ nm (a, upper inset) and the $InP/GaInP_2$ structure (a, lower inset); and surface potential (top) and surface relief (bottom) maps of GaN layers grown at the flux ratios of $Ga/N_2 \cdot 1.1$ (b) and 1.3 (c). (A color version of the figure is provided in the online version of the paper).

density decreases by a factor of 2, and they become an order of magnitude deeper (see the lower inset in Figure 1, a).

The measured potential relief of the GaN layer grown at a flux ratio of $Ga/N_2 \cdot 1.1$ (see Figure 1, a, upper panel) reveals $U_{s0} \sim 0.7$ V and the presence of SPWs $0.2-1\,\mu m$ in size with ΔU_s up to 0.15 V and a density of $0.5\,\mu m^{-2}$, which are induced by inversion domains (IDs). The layer has a granular surface with a grain size of $\sim 1\,\mu m$ and a height of ~ 30 nm (see Figure 1, b, lower panel). The adhesion of $1M$-WSe_2 flakes to this layer was weak. This led to their detachment from the layer and is likely attributable to the granular structure of the surface. Gallium droplets (GDs) in the layer with a flux ratio of 1.3 yield SPWs with ΔU_s up to 0.2 V (see Figure 1, c, upper panel), and the layer surface is smoothed out between these droplets. The density of IDs increases in this case, and they merge into regions as large as several micrometers in diameter. $1M$-WSe_2 flakes were transferred successfully in experiments with this layer.

3.2. Surface potential of 1M-WSe_2 structures

Figures 2, $a-d$ present the optical images ($\sim 20 \times 40\,\mu m$ in size) and surface potential maps ($10 \times 10\,\mu m$ in size) of $1M$-WSe_2 flakes on $GaInP_2$, $InP/GaInP_2$, GaN, and SiO_2. The size of transferred flakes varies from $\sim 5 \times 15\,\mu m$ for $InP/GaInP_2$, $\sim 10 \times 25\,\mu m$ for $GaInP_2$, and $\sim 20 \times 40\,\mu m$ for SiO_2 to $\sim 35 \times 65\,\mu m$ for GaN (see Figure 4 below); therefore, only a part of a flake is visible in the optical image for GaN.

In the case of $GaInP_2$, the optical image of a $1M$-WSe_2 flake (see Figure 2, a) reveals transfer defects: cracks (transverse dark stripes), scotch residue (light longitudinal stripes with a width of $\sim 1\,\mu m$), and a $2M$-WSe_2 fragment (at the top). The U_{s0} value for a 1M flake is 1.4 V, which is 0.1 V lower than U_{s0} of the $GaInP_2$ substrate (1.5 V) induced by a 10 kV/cm built-in electric field (see Figure 1, a). The flake potential has a fine relief with amplitude $\Delta U_s < 0.01$. A feature with $\Delta U_s \sim \pm 0.02$ V along the defects is also visible. The SiO_2 substrate (Figure 2, d) has similar defects; the corresponding U_{s0} decreases by almost 2 V to -0.5 V. In this case, U_{s0} of the substrate assumes the value of -0.9 V.

A $1M$-WSe_2 flake on $InP/GaInP_2$ (Figure 2, b) is not visible in the optical image and was identified by examining the surface potential map (see Figure 2, b, lower panel). The U_{s0} value of the flake (1.3 V) is 0.3 V lower than that of the substrate (1.5 V) and decreases to 1.2 V toward the edges. The potential relief is formed by „humps“ with a height of 0.2 V, a size of ~ 200 nm, and a density of $5\,\mu m^{-2}$ produced by InP quantum dots.

In the case of GaN (see Figure 2, c), the optical image of a $1M$-WSe_2 flake reveals ruptures in the center and at the top (dark stripes $1-2\,\mu m$ in width). The flake is thus divided into three parts: the upper triangular one with a size of $\sim 10\,\mu m$ and two central parts with a cut in the middle, which are not shown fully in the image. The flakes have a granular structure with a grain size of $\sim 1\,\mu m$. The left and upper flakes are superimposed onto GDs (light spots) ~ 1 and $2\,\mu m$ in diameter. The measurements of U_s revealed that the flake potential follows the substrate potential (see Figures 1, c and 4, d below). Figure 2, c shows a 0.05-V-deep ID SPW located in the lower part of the left flake, which is marked with a dotted circle. GD SPWs have $\Delta U_s \sim 0.1$ V and are $\sim 1\,\mu m$ in size (see below).

3.3. Raman spectra of 1M-WSe_2 structures

The Raman spectra of all four substrates, which are presented within the $230-290\,cm^{-1}$ range in Figures 3, $a-d$, featured an intense (~ 1000 cps, cost per sale) peak of longitudinal optical phonon A'_1 of $1M$-WSe_2 with maximum $\nu_{A'1} \sim 251\,cm^{-1}$ and width $\gamma_{A'1} \sim 4\,cm^{-1}$ and a weaker overtone of the longitudinal acoustical phonon ($\sim 264\,cm^{-1}$) [23]. Variations $\Delta\nu_{A'1}$ and $\Delta\gamma_{A'1}$ over the area of flakes depend only weakly on the substrate type and are $\sim 1\,cm^{-1}$ in magnitude. SiO_2, however, has a slightly greater $\Delta\nu_{A'1}$ ($\sim 1.5\,cm^{-1}$), which is apparently attributable

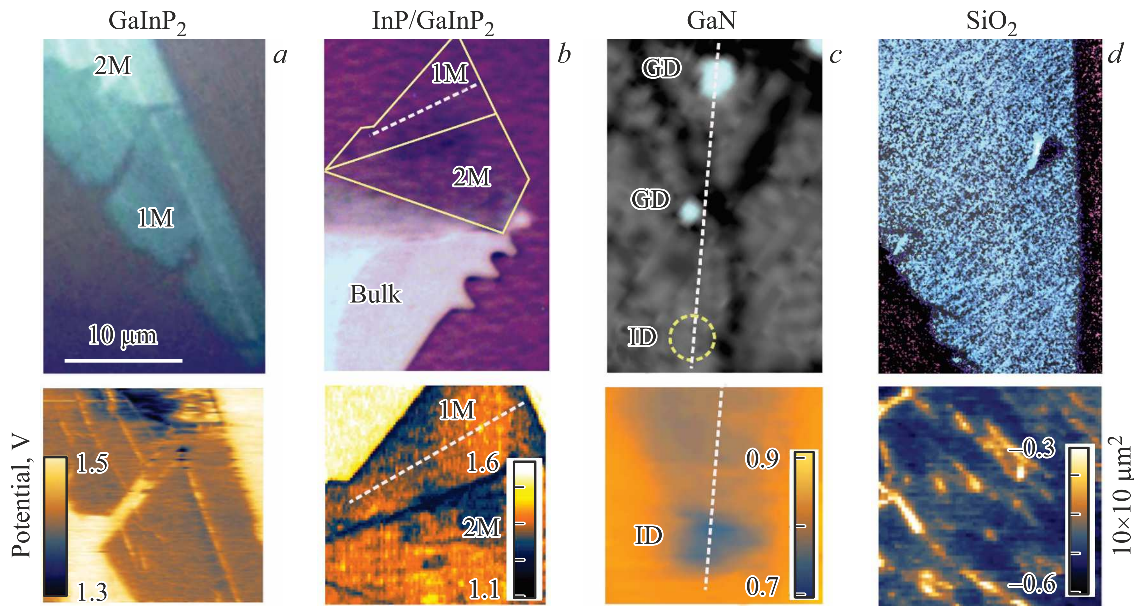

Figure 2. Optical images and surface potential map (lower insets) of WSe_2 flakes on $GaInP_2$ (*a*), $InP/GaInP_2$ (*b*), GaN (*c*), and SiO_2 (*d*). Solid lines in panel (*b*) represent the boundaries of 1M and 2M flakes determined from the surface potential map (see the inset below); dashed straight lines in panels (*b*) and (*c*) are the lines (axis *x*) along which the dependences in Figures 3, *b–e* are plotted. Gallium droplets (GD) and the inverse domain (ID), which is denoted with a dotted circle (see potential map in the lower inset), are indicated in panel (*c*).

to the higher density of scotch tape residue (see Figure 2, *d*, bottom panel). Variations $\Delta\nu_{A'1}$ correspond to elastic strain variations $\Delta\varepsilon \sim 0.4\%$ [24].

Intensity variations (see the $I_{A'1}$ maps in the insets on the right) $\Delta I_{A'1} < 0.1$ for SiO_2 and $GaInP_2$ and 0.4–4 for $InP/GaInP_2$ and GaN; thus, $\Delta I_{A'1} \sim \Delta U_s$. Figures 3, *b–e* show the variations of $\nu_{A'1}$, $I_{A'1}$, U_s, and the surface height for $InP/GaInP_2$ and GaN along the lines going through the InP dots and ID/GD regions with the greatest ΔU_s (see the maps in Figures 2, *b* and *c*). It is evident that $I_{A'1}$ and U_s are inversely proportional to each other and have the same spatial variations. Specifically, the potential humps in $InP/GaInP_2$ with a spatial size of $\sim 0.2\,\mu$m found within the $x = 6-8\,\mu$m coordinate range correspond to the $I_{A'1}$ minima with a relative amplitude of 0.4; in GaN, the potential wells $\sim 1.5\,\mu$m in size located at points $x = 16$, 27, 33, and $36\,\mu$m correspond to the $I_{A'1}$ maxima with a relative amplitude ranging from 0.4 (for the GD at $x = 27\,\mu$m and the ID at $33\,\mu$m) to 4 (for the ID at $x = 16\,\mu$m and the GD at $x = 33\,\mu$m). The 4-fold enhancement of the Raman scattering intensity for IDs and GDs is unexpected. In the former case, this enhancement is represented by a bright spot several micrometers in size that is visible in the corresponding map in Figure 3, *a*. This „giant“ enhancement is not related to local strain and surface roughness, since the A'_1 phonon frequency in these regions changes by $< 0.2\,\mathrm{cm}^{-1}$ (see Figure 3, *b*). The indicated value is significantly smaller than the variations of $\nu_{A'1}$ in all samples with different surface relief (see Figure 3, *e*) and corresponds to an elastic strain variation $< 0.1\%$. Note that the ID and GD located at points $x = 27$ and $33\,\mu$m, respectively, feature „weak“ enhancement, which may be attributed to their smaller size (see the topography map in Figure 3, *e*).

3.4. Exciton spectra and local doping of 1M-WSe_2

Exciton emission peak AEX of 1M-WSe_2 with maximum $\lambda_{AEX} = 749$ nm and $\gamma_{AEX} = 24$ nm [25,26] was observed in the PL spectra (see Figure 4, *a*) for $GaInP_2$, GaN, and SiO_2. The maps in the insets reveal I_{AEX} intensity variations with a magnitude of approximately 50%, which are attributable to defects and the granular structure of flakes. The magnitude of $\Delta\lambda_{AEX}$ variations is ~ 5 nm and is consistent with the value of $\Delta\varepsilon \sim 0.4\%$ [24,27]. In the case of $InP/GaInP_2$, this range is dominated by the emission of InP dots, which is suppressed by the flake (see the corresponding map). GaN has $\Delta\lambda_{AEX} = 20$ nm, which is induced by the regions where the A_{TR} trion peak with $\lambda_{ATR} = 770$ nm and $\gamma_{ATR} = 30$ nm [26] (see Figure 4, *a*) is dominant. These regions are seen as bright spots in the 770 nm PL intensity maps (I_{ATR}) and the PL peak position (λ_A) maps presented in Figures 4, *b* and *c*, respectively, and are localized in GD- and ID-induced SPW regions of the U_s map in Figure 4, *d*. The dominance of A_{TR} is indicative of local doping to the $n \sim 10^{12}\,\mathrm{cm}^{-2}$ level and is consistent with the presence of SPWs in these regions.

Thus, the giant enhancement of the $I_{A'1}$ Raman scattering intensity in the ID and GD regions is due to doping. Our analysis indicates that this enhancement is associated with

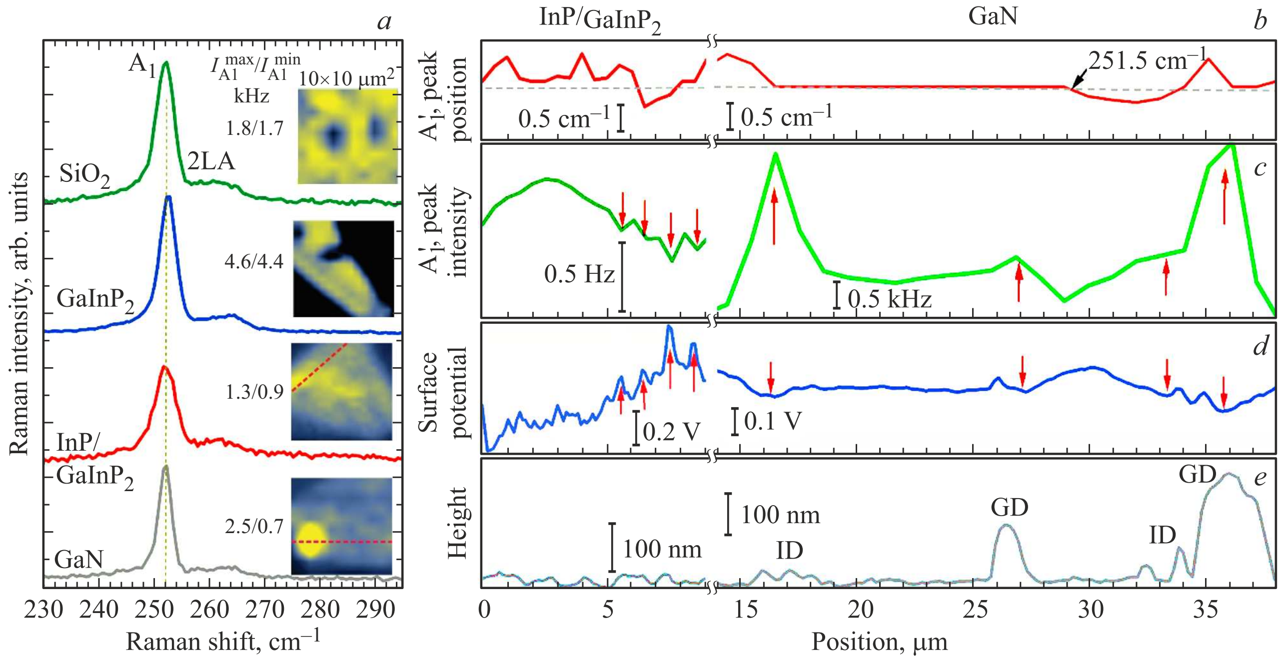

Figure 3. (*a*) Raman spectra and intensity maps of the A_1' peak in these spectra (insets on the right) for 1M-WSe_2 on SiO_2, $GaInP_2$, InP/$GaInP_2$, and GaN. Spatial variations of position (*b*) and intensity (*c*) of the A_1' peak alongside with variations of the surface potential (*d*) and relief (*e*) for InP/$GaInP_2$ (left) and GaN (right) along the lines shown in the insets on the right and Figures 2, *b* and *c*, respectively.

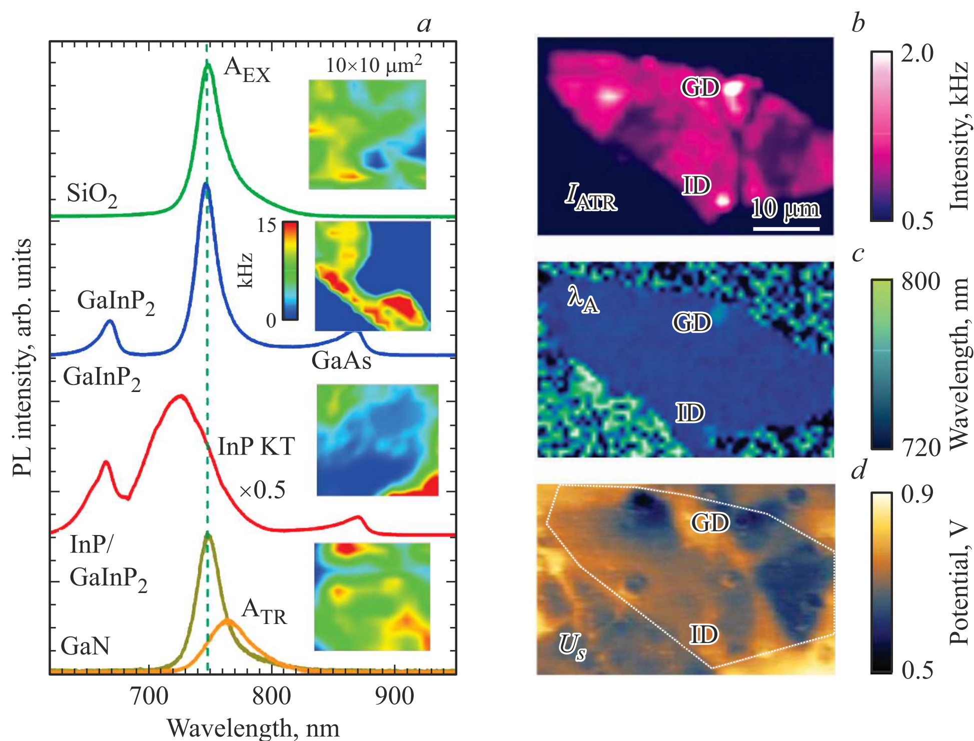

Figure 4. (*a*) PL spectra and AEX peak intensity maps (insets on the right) for 1M-WSe_2 on SiO_2, $GaInP_2$, InP/$GaInP_2$, and GaN. Maps of PL intensity IATR of the trion peak (*b*), PL peak maximum wavelength λ_A (*c*), and surface potential U_s (*d*) of a 1M-WSe_2 flake on GaN. The dotted outline in panel (*d*) represents the boundaries of the flake.

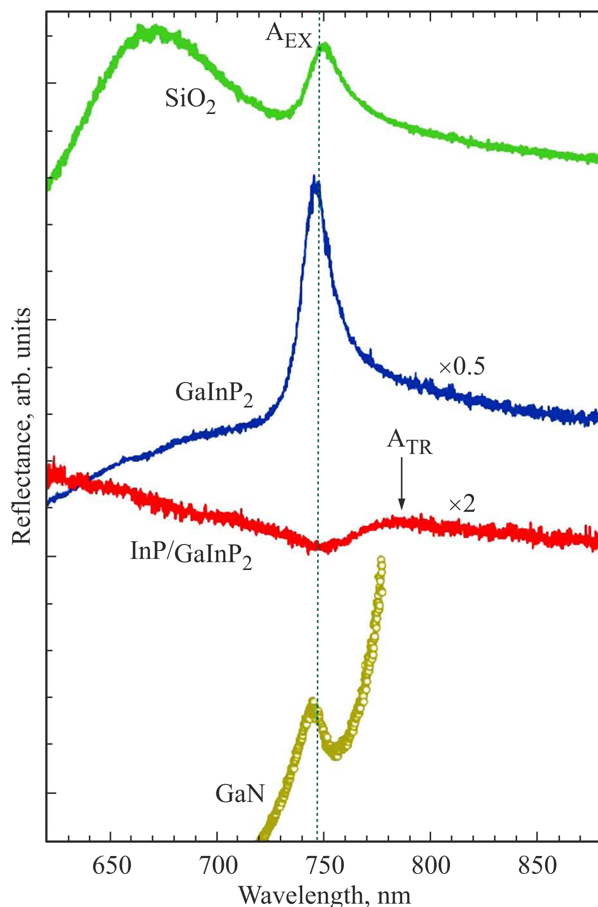

Figure 5. Reflectance spectra for 1M-WSe_2 on SiO_2, $GaInP_2$, InP/$GaInP_2$, and GaN.

resonance conditions under which the excitation energy is detuned by 0.2 eV toward lower energies from the maximum of the resonant exciton transition [28]. In the case of doping, the formation of a trion results in a red shift of the resonant transition maximum and a corresponding reduction of the detuning magnitude. Thus, the variations of $I_{A'1}$ observed in Figure 3, d are due to local changes in density n. The suppression of $\Delta I_{A'1}$ observed for smaller GDs and IDs on GaN (see Figure 3, e) is indicative of a reduction in n, and the variations of $I_{A'1}$ and its decrease at the InP/$GaInP_2$ potential humps are indicative of doping of the entire 1M-WSe_2 layer and the formation of „antidots“. The doping of 1M-WSe_2/InP/$GaInP_2$ is evident from the reflectance spectrum (see Figure 5): in contrast to the spectra of other structures with visible exciton peaks, it features a trion peak with $\lambda_{ATR} = 780$ nm and $\gamma_{ATR} = 80$ nm.

Note that the possibility of shifting the exciton wavelength to 770 nm for GDs and IDs due to local elastic strain, which is what is observed in structures with profiled substrates [29–31], is excluded due to the smallness of $\Delta\nu_{A'1} < 0.2\,\mathrm{cm}^{-1}$ (see Figure 3, b) and the presence of SPWs.

The doping of 1M-WSe_2 is attributable to the presence of the corresponding electronic surface states. In the case of InP/$GaInP_2$, these states are induced by local strain of InP dots, which follows from the lack of doping for $GaInP_2$. In the case of GaN, doping is observed for GDs and IDs located near the edge, indicating that these states are associated with dangling W-Se bonds that accumulate electrons.

4. Conclusion

Kelvin scanning probe microscopy and optical spectroscopy (photoluminescence, Raman scattering, reflectance) measurements of WSe_2 monolayers transferred onto $GaInP_2$, InP/$GaInP_2$, GaN, and SiO_2 epitaxial layers were used to study the influence of piezoelectric substrate inhomogeneities on local WSe_2 doping. A correlation between the intensity of resonant Raman scattering by optical phonon A'_1, the intensity of emission of a charged exciton (trion), and the surface potential variations induced by piezoelectric inhomogeneities was found for InP/$GaInP_2$ and GaN. Correlation analysis revealed local doping of monolayer WSe_2 at the $n \sim 10^{12}\,\mathrm{cm}^{-2}$ level and the $0.2-1.5\,\mu$m length scale. The obtained results demonstrate the possibility of production of Wigner quantum dot structures in transition metal dichalcogenides, opening up new prospects for fault-tolerant topological quantum computing.

Funding

The study of piezoelectric fields in structures was supported by grant No. 24-29-00375 from the Russian Science Foundation.

Conflict of interest

The authors declare that they have no conflict of interest.

References

[1] F. Wilczek. Phys. Rev. Lett., **49** (14), 957 (1982). DOI: 10.1103/PhysRevLett.49.957
[2] A.Y. Kitaev. Annals of Physica, **303** (1), 2 (2003). DOI: 10.1016/S0003-4916(02)00018-0
[3] S.D. Sarma, M. Freedman, C. Nayak. npj Quant. Information, **1** (15001), 1 (2015). DOI: 10.1038/npjqi.2015.1
[4] A.M. Mintairov, D.V. Lebedev, A.S. Vlasov, A.O. Orlov, G.L. Snider, A. Blundell. Sci. Rep., **12**, 21440−14 (2021). DOI: 10.1038/s41598-021-00859-6
[5] D.C. Tsui. H.L. Stormer, A.C. Gossard. Phys. Rev. Lett., **48** (22), 1559 (1982). DOI: 0.1103/PhysRevLett.48.1559
[6] D. Monroe, Y.H. Xie, E.A. Fitzgerald, P.J. Silverman. Phys. Rev. B, **46** (12), 7935 (1992). DOI: 10.1103/PhysRevB.46.7935
[7] A. Tsukazaki, S. Akasaka, K. Nakahara, Y. Ohno, H. Ohno, D. Maryenko, A. Ohtomo, M. Kawasaki. Nature Materials, **9**, 889 (2010). DOI: 10.1038/nmat2874

[8] M.J. Manfra, N.G. Weimann, J.W.P. Hsu, L.N. Pfeiffer, K.W. West, S. Syed, H.L. Stormer, W. Pan, D.V. Lang, S.N.G.Chu, G. Kowach, A.M. Sergent, J. Caissie, K.M. Molvar, L.J. Mahoney, R.J. Molnar. J. Appl. Phys., **92** (1), 338 (2002). DOI: 10.1063/1.1484227
[9] K.S. Novoselov, D. Jiang, F. Schedin, T.J. Booth, V.V. Khotkevich, S.V. Morozov, A.K. Geim. PNAS, **102** (30), 10451 (2005). DOI: 10.1073/pnas.050284810210451
[10] X. Du, I. Skachko, F. Duerr, A. Luican, E.Y. Andrei. Nature, **462** (12), 192 (2009). DOI: 10.1038/nature08522
[11] Q. Shi, E.-M. Shih, M.V. Gustafsson, D.A. Rhodes, B. Kim, K. Watanabe, T. Taniguchi, Z. Papić, J. Hone, C.R. Dean. Nature Nanotechnol., **15**, 569 (2020). DOI: 10.1038/s41565-020-0685-6
[12] S. Kumar, M. Pepper, S.N. Holmes, H. Montagu, Y. Gul, D.A. Ritchie, I. Farrer. Phys. Rev. Lett., **122** (8), 086803−5 (2019). DOI: 10.1103/PhysRevLett.122.086803
[13] J.-X. Yin, Z. Wu, J.-H. Wang, Z.-Y. Ye, J. Gong, X.-Y. Hou, L. Shan, A. Li, X.-J. Liang, X.-X. Wu, J. Li, C.-S. Ting, Z.-Q. Wang, J.-P. Hu, P.-H. Hor, H. Ding, S. H. Pan. Nature Physics, **11**, 543 (2015). DOI: 10.1038/nphys3371
[14] K.F. Mak, K. He, C. Lee, G.H. Lee, J. Hone, T.F. Heinz, J. Shan. Nature Materials, **12**, 207 (2013). DOI: 10.1038/nmat3505
[15] J. Boddison-Chouinard, A. Bogan, N. Fong, K. Watanabe, T. Taniguchi, S. Studenikin, A. Sachrajda, M. Korkusinski, A. Altintas, M.Bieniek, P. Hawrylak, A. Luican-Mayer, L. Gaudreau. Appl. Phys. Lett., **119** (13), 133104 (2021). DOI: 10.1063/5.0062838
[16] S. Davari, J. Stacy, A.M. Mercado, J.D. Tull, R. Basnet, K. Pandey, K. Watanabe, T. Taniguchi, J. Hu, H.O.H. Churchill1. Phys. Rev. Appl., **13**, 054058−8 (2020). DOI: 10.1103/PhysRevApplied.13.054058
[17] F. Riche, H. Braganc, F. Qu, V. Lopez-Richard, S.J. Xie, A.C. Dia, G.E. Marques. J. Phys.: Condens. Matter, **32**, 365702−10 (2020). DOI: 10.1088/1361-648X/ab8fd4
[18] A.V. Ankudinov, N.A. Bert, M.S. Dunaevskiy, A.I. Galimov, N.A. Kalyuzhnyy, S.A. Mintairov, A.V. Myasoedov, N.V. Pavlov, M.V. Rakhlin, R.A. Salii, A.A. Toropov, A.S. Vlasov, E.V. Pirogov, M.A. Zhukovskyi, A.M. Mintairov. Appl. Phys. Lett., **124**, 052101 (2024). DOI: 10.1063/5.0172579
[19] A.M. Mintairov, J. Kapaldo, J.L. Merz, S. Rouvimov, D.V. Lebedev, N.A. Kalyuzhnyy, S.A. Mintairov, K.G. Belyaev, M.V. Rakhlin, A.A. Toropov, P.N. Brunkov, A.S. Vlasov, Yu.M. Zadiranov, S.A. Blundell, A.M. Mozharov, I. Mukhin, M. Yakimov, S. Oktyabrsky, A.V. Shelaev, V.A. Bykov. Phys. Rev. B, **97** (97), 195443−9 (2018). DOI: 10.1103/PhysRevB.97.195443
[20] A.M. Mintairov, A.V. Ankundinov, N.A. Kalyuzhnyy, D.V. Lebedev, S.A. Mintairov, N.V. Pavlov, A.I. Galimov, M.V. Rakhlin, R.A. Salii, A.A. Toropov, A.S. Vlasov, D. Barettin, M. Auf der Maur, S.A. Blundell. Appl. Phys. Lett., **118**, 121101−6 (2021). DOI: 10.1063/5.0045925
[21] V.N. Jmerik, D.V. Nechaev, S.V. Ivanov. *In Molecular Beam Epitaxy: From research to mass production*, ed. by M. Henini. 2nd edn (Elsevier Inc., 2018) p. 135.
[22] A.M. Mintairov, J.L. Merz, A.S. Vlasov. Phys. Rev. B, **67** (20), 205211-7 (2003). DOI: 10.1103/PhysRevB.67.205211
[23] H. Terrones, E. Del Corro, S. Feng, J.M. Poumirol, D. Rhodes, D. Smirnov, N.R. Pradhan, Z. Lin, M.A.T. Nguyen, A.L. El´ıas, T.E. Mallouk, L. Balicas, M.A. Pimenta, M. Terrones. Sci. Rep., **4**, 4215−9 (2014). DOI: 10.1038/srep04215
[24] S. Roy, X. Yang, J. Gao. Adv. Photon. Res., **5** (4), 2300220−6 (2024). DOI: 10.1002/adpr.202300220
[25] K. He, N. Kumar, L. Zhao, Z. Wang, K. Fai Mak, H. Zhao, J. Shan. Phys. Rev. Lett., **113**, 026803−5 (2014). DOI: 10.1103/.113.026803
[26] T.Y. Jeong, S.-Y. Lee, S. Jung, K.J. Yee. Current Appl. Phys., **20** (2), 272 (2020). DOI: 10.1016/j.cap.2019.11.016
[27] B. Aslan, M. Deng, T.F. Heinz. Phys. Rev. B, **98** (11), 15308−6 (2018). DOI: 10.1103/PhysRevB.98.115308
[28] E. de Coro, H. Terrones, A. Elias, C. Fantini, S. Feng, M.A. Nguyen, T.E. Mallouk, M. Terrones, M.A. Pimenta. ACS Nano, **8** (9), 9629 (2014). DOI: 10.1021/nn504088g
[29] H. Li, A.W. Contryman, X. Qian, S.M. Ardakani, Y. Gong, Xi. Wang, J.M. Weisse, C.H. Lee, J. Zhao, P.M. Ajayan, J. Li, H.C. Manoharan, X. Zheng. Nature Commun., **6**, 7381−6 (2015). DOI: 10.1038/ncomms8381
[30] A. Branny, S. Kumar, R. Proux, B.D. Gerardot. Nature Commun., **8**, 15053−7 (2017). DOI: 10.1038/ncomms15053
[31] C. Palacios-Berraquero, D.M. Kara, A.R.-P. Montblanch, M. Barbone, P.l. Latawiec, D. Yoon, A.K. Ott, M. Loncar, A.C. Ferrari, M. Atatüre. Nature Commun., **8**, 15093−6 (2017). DOI: 10.1038/ncomms15093

Translated by D.Safin